

**SARS-CoV-2 disease severity and transmission efficiency is increased for airborne but not fomite exposure in Syrian hamsters.**

Julia R. Port<sup>1\*</sup>, Claude Kwe Yinda<sup>1\*</sup>, Irene Offei Owusu<sup>1</sup>, Myndi Holbrook<sup>1</sup>, Robert Fischer<sup>1</sup>, Trenton Bushmaker<sup>1,2</sup>, Victoria A. Avanzato<sup>1</sup>, Jonathan E. Schulz<sup>1</sup>, Neeltje van Doremalen<sup>1</sup>, Chad S. Clancy<sup>3</sup>, Vincent J. Munster<sup>1#</sup>

1. Laboratory of Virology, Division of Intramural Research, National Institutes of Health, Hamilton, MT, USA
2. Montana State University, Bozeman, Montana, USA
3. Rocky Mountain Veterinary Branch, Division of Intramural Research, National Institutes of Health, Hamilton, MT, USA

\*“These authors contributed equally to this work”

#Corresponding author: Vincent Munster, email: [vincent.munster@nih.gov](mailto:vincent.munster@nih.gov)

## **Abstract (150 words or less)**

Transmission of SARS-CoV-2 is driven by contact, fomite, and airborne transmission. The relative contribution of different transmission routes remains subject to debate. Here, we show Syrian hamsters are susceptible to SARS-CoV-2 infection through intranasal, aerosol and fomite exposure. Different routes of exposure presented with distinct disease manifestations. Intranasal and aerosol inoculation caused more severe respiratory pathology, higher virus loads and increased weight loss. Fomite exposure led to milder disease manifestation characterized by an anti-inflammatory immune state and delayed shedding pattern. Whereas the overall magnitude of respiratory virus shedding was not linked to disease severity, the onset of shedding was. Early shedding was linked to an increase in disease severity. Airborne transmission was more efficient than fomite transmission and dependent on the direction of the airflow. Carefully characterized of SARS-CoV-2 transmission models will be crucial to assess potential changes in transmission and pathogenic potential in the light of the ongoing SARS-CoV-2 evolution.

**Keywords:** SARS-CoV-2, animal model, hamster, transmission, coronavirus

## Introduction

Since the emergence of severe acute respiratory syndrome coronavirus-2 (SARS-CoV-2) in Wuhan, China, in December 2019, the virus has spread across the globe and has caused over 70 million cases and 1.5 million deaths as of December 2020 [1]. Infection with SARS-CoV-2 can cause asymptomatic to severe lower respiratory tract infections in humans [2, 3]. Peak respiratory shedding in humans occurs at the time of symptom onset or in the week thereafter, followed by a steady decline after the induction of a humoral immune response [4]. To a lesser extent, shedding from the intestinal tract has also been observed, but generally does not appear to be associated with the presence of infectious SARS-CoV-2 nor subsequent transmission. There is no established relationship between COVID-19 disease severity and duration and magnitude of SARS-CoV-2 shedding [5].

Considering the scale of the COVID-19 pandemic, it remains unclear to what extent the different routes of exposure contribute to human-to-human transmission and how the exposure route affects disease manifestation. In order to evaluate existing SARS-CoV-2 control measures it is crucial to understand the relative contribution of different transmission routes. Because the majority of cases have been observed in households or after social gatherings, transmission of SARS-CoV-2 is believed to be driven mostly by direct contact, fomites, and short-distance airborne transmission [6]. Airborne transmission can be defined as human-to-human transmission through exposure to large droplets and small droplet nuclei that can be transmitted through the air; whereas airborne transmission includes transmission through both large and small droplets, true aerosol transmission occurs via droplet nuclei particles smaller than 5  $\mu\text{m}$ . Fomites are a result of infectious respiratory secretions or droplets being expelled and contaminating surfaces.

In multiple hospital settings SARS-CoV-2 viral RNA has been consistently detected on surfaces [7-12] and air-samples [8, 9, 13-20]. Detection of infectious virus in air and surface samples has been relatively limited, however infectious SARS-CoV-2 has been recovered from air samples

[21] and surfaces [22, 23]. Experimental research has shown viral RNA can consistently be detected for up to seven days on surfaces but, the infectious virus degrades rapidly, with limited presence after two days [12]. This discrepancy between the consistent detection of SARS-CoV-2 viral RNA and the relatively short time frames when viable virus can be detected directly hampers our ability to translate SARS-CoV-2 RNA detection on hospital surfaces and in air samples to understanding transmission and relative contribution of fomites and airborne virus. In the current study we use the well-established Syrian hamster model [24-26] to experimentally delineate the relative contribution of fomite and airborne transmission and study the impact of transmission route on disease severity using this model. We evaluated the SARS-CoV-2 tropism, shedding profile, disease severity and immune response after different exposures. Using this data, we developed a hamster airborne and fomite transmission model to confirm our findings in a natural transmission setting.

## Results

### Clinical disease severity is correlated with exposure route

To investigate the impact of exposure route on disease severity, we compared three different inoculation routes. Three groups of 12, 4-6-week-old, female hamsters were inoculated with SARS-CoV-2 via the intranasal (I.N.;  $8 \times 10^4$  TCID<sub>50</sub>), aerosol ( $1.5 \times 10^3$  TCID<sub>50</sub>) or fomite ( $8 \times 10^4$  TCID<sub>50</sub>) routes (Fig 1 a). An unexposed control was included (N = 12) as comparison. For each group, 4 animals were euthanized on 1 day post inoculation (DPI) and 4 DPI, the remaining 4 animals were monitored until 14 DPI. Animals inoculated via the I.N. or aerosol routes demonstrated significant weight loss, whereas fomite exposure resulted in limited, transient weight loss. Animals inoculated I.N. started losing weight at 3 DPI and aerosol exposed animals at 2 DPI (Fig 1 b). Weight loss at 6 DPI was significant compared to unexposed controls for I.N., and at 4 DPI for aerosol group (Fig 1 b; N = 4, Mann-Whitney test,  $p = 0.0286$  and  $p = 0.0286$ ). In addition to weight loss, inconsistent, temporary, mild lethargy and ruffled fur were observed.



Fomite exposure presented with less weight gain compared to unexposed controls. At 14 DPI no significant difference was observed between the groups (Fig 1 c; N = 4, Kruskal-Wallis test, followed by Dunn's multiple comparison test,  $p = 0.2953$ ).

# **Aerosol exposure directly deposits virus in the upper and lower respiratory tract, with replication in the nasal cavity epithelium, tracheal and bronchial epithelia**

Early (1 DPI) SARS-CoV-2 tropism and replication were investigated for each exposure route. Infectious virus could be detected in the trachea of all I.N. and aerosol exposed animals. In the lung, infectious virus was detected in all aerosol exposed animals and a subset of I.N. inoculated hamsters (Fig 1 d). No infectious virus was detected at 1 DPI in the fomite group in either the upper or lower respiratory tract. Compared to I.N. exposed animals, aerosol exposed hamsters demonstrated significantly increased viral load in the trachea and the lung at this time point (N = 4, ordinary two-way ANOVA, followed by Tukey's multiple comparisons test,  $p = 0.0115$  and  $p = <0.0001$ , respectively). This suggests that aerosol exposure more efficiently deposits viral droplet nuclei in the lower respiratory system. No infectious virus was detected in the gastrointestinal tract regardless of the route of inoculation.

To investigate initial cellular tropism, immunohistochemistry (IHC) targeting the SARS-CoV-2 nucleoprotein as a marker of SARS-CoV-2 replication was performed on skull sagittal sections and lung sections at 1 DPI. In aerosol inoculated animals, viral antigen was observed in moderate to numerous ciliated epithelial cells in the nasal cavity, tracheal mucosa, and bronchiolar mucosa. In addition, viral antigen was detected in type I and type II pneumocytes, pulmonary macrophages and olfactory epithelial cells (Fig 2 a, e, i, m). Comparatively, evaluation of I.N. exposed hamsters revealed a lack of viral antigen in the epithelial cells of the trachea and lung at this timepoint. Interestingly, viral antigen was detected in pulmonary macrophages in a subset (N= 2/4) of I.N. inoculated hamsters at 1 DPI. Viral antigen was detected in ciliated and olfactory epithelium of the nasal turbinates (Fig 2 b, f, j, m). In

accordance with the virological findings, no SARS-CoV-2 antigen was detected in the trachea or lung of any fomite inoculated hamsters (N = 0/4). Viral antigen was detected in ciliated epithelial cells of the nasal turbinates in one (N = 1/4) fomite inoculated hamster (Fig 2 c, g, k, m). No SARS-CoV-2 antigen was detected in the esophagus or brain in any of the evaluated animals (data not shown) nor in unexposed control tissues (Fig 2 d, h, l, m).

### **Fomite SARS-CoV-2 exposure displays delayed replication kinetics in the respiratory tract and leads to less severe lung pathology**

To determine the correlation between exposure route and subsequent respiratory tract pathology, sections of lung, trachea and nasal turbinates were obtained for histopathological evaluation at 1 and 4 DPI. Interestingly, nasal turbinate pathology was observed in a subset of hamsters regardless of inoculation route at 1 DPI (Fig 3 a, b, c). Histopathologic lesions were observed primarily in ciliated epithelial cells at 1 DPI and were most consistently observed in the I.N. inoculation group with all (N = 4/4) inoculated animals exhibiting mild to moderate ciliated epithelial cell necrosis with influx of numerous degenerate and non-degenerate leukocytes followed closely by aerosol inoculated hamsters with 75% (N = 3/4) exhibiting minimal to moderate pathology. The fomite inoculation group had the least consistent and least severe histopathologic lesions in the nasal turbinates with half (N = 2/4) of hamsters having no histopathologic lesions and the remaining hamsters (N = 2/4) having only minimal pathology. Mild to moderate tracheal inflammation was observed in all (N = 4/4) aerosol inoculated and half (N = 1/2) of the I.N. inoculated hamsters (Fig 3 e, f). Tracheal inflammation was not observed in any of the fomite inoculated hamsters (N = 4; Fig 3 g), confirming that virus titers detected at 1 DPI are linked to early-onset pathological changes in this model. As expected, pulmonary pathology was minimal (aerosol and fomite) at 1 DPI, regardless of route of inoculation. Early histopathologic lesions in the lung included rare single cell bronchiolar epithelial cell necrosis, infiltration of rare or low numbers of neutrophils into the bronchiolar mucosa and focal interstitial

pneumonia with minimal septal expansion by edema fluid and spillover of rare leukocytes into the adjacent alveolar spaces (Fig 3 i, j, k).

By 4 DPI, infectious virus could be detected in the lung of all animals regardless of inoculation route. No significant difference was observed between I.N. and aerosol or fomite exposed animals (Fig 1 d; N = 4, ordinary two-way ANOVA, followed by Tukey's multiple comparisons test,  $p = 0.4114$  and  $p = 0.9201$ , respectively). An increase in the severity of both turbinate and pulmonary pathology was observed in all evaluated hamsters regardless of the route of inoculation. Interestingly, in both aerosol and I.N. inoculation routes, regions of olfactory epithelium within the nasal turbinates were more severely affected, suggesting initial viral attachment and replication in ciliated epithelium followed by targeting of the more caudal olfactory epithelium during disease progression (Fig 3 m, n, o). At this timepoint, nasal mucosal pathology was observed in all fomite inoculated animals. However, the pathology was less severe as compared to I.N. and aerosol groups and focused primarily on regions of ciliated mucosa, suggesting a delay in disease progression relative to aerosol and I.N. routes. Tracheal inflammation was observed in all inoculation routes and varied from minimal to mild (Fig 3 q, r, s). Moderate pulmonary pathology consistent with previously described SARS-CoV-2 infection in Syrian hamsters [24] was observed in aerosol and I.N. inoculated animals at 4 DPI (Fig 3 u, v) with less severe and less consistent pathology observed in the fomite inoculation group (Fig 3 w). Lesions were characterized as moderate, broncho-interstitial pneumonia centered on terminal bronchioles and extending into adjacent alveoli. The interstitial pneumonia was characterized by thickening of alveolar septa by edema fluid, fibrin and moderate numbers of macrophages and fewer neutrophils. Inconsistent pulmonary pathology was observed for this group with lesions ranging from minimal to moderate, which is in accordance with the observation that some fomite exposed animals did demonstrate high viral loads in the lung at 4 DPI (Fig 3 w). No significant histopathologic lesions were observed in sections of mediastinal

and mesenteric lymph node, esophagus, duodenum, or colon, (data not shown) or any control animal on 1 and 4 DPI (Fig 3 d, h, l, p, t, x).

Using a hierarchical clustering of lung pathology parameters (bronchiolitis, interstitial pneumonia, tracheitis, pathology of the ciliated and olfactory epithelium) on both 1 and 4 DPI in relation to the observed viral titers, a clear relationship existed between the respiratory pathology at 1 DPI in the trachea, and viral load of trachea and lung, while pathology in the nasal epithelial was more distantly related (Fig 3 y). Of note, viral load in the lungs at 4 DPI was most closely associated with presentation of interstitial pneumonia. Fomite exposed animals most closely resembled unexposed controls at 1 DPI and clustered together as a separate group at 4 DPI due to the appearance of tracheitis, pathology in the ciliated epithelium without distinct lower respiratory tract involvement (Fig 3 z). This implies that fomite SARS-CoV-2 exposure displays delayed replication kinetics in the respiratory tract and leads to less severe lung pathology at 4 DPI compared to direct deep deposition of virus into the respiratory tract (aerosol inoculation).

## **Fomite SARS-CoV-2 exposure results in a delayed, reduced, and anti-inflammatory immune profile**

To investigate the systemic immune response, cytokine specific ELISAs were performed on serum at 4 DPI (Fig 4 a). Expression patterns were strikingly different depending on exposure route for pro-inflammatory tumour necrosis factor (TNF)- $\alpha$  and anti-inflammatory IL-4 and IL-10. Both I.N. and aerosol groups presented with increased levels of TNF- $\alpha$  at 4 DPI as compared to unexposed animals, whilst the fomite exposed group demonstrated decreased levels; a significant difference in serum levels was detected between I.N. and fomite exposed groups ( $N = 4$ , Kruskal-Wallis test, followed by Dunn's multiple comparisons test,  $p = 0.0360$ ). Adversely, the IL-4 levels were markedly increased in all groups as compared to unexposed animals, yet

highest levels were seen in fomite exposed animals, the difference between unexposed and fomite group reaching statistical significance (N = 4, Kruskal-Wallis test, followed by Dunn's multiple comparisons test,  $p = 0.0109$ ). Increased serum IL-10 was also observed in fomite exposed animals and I.N. exposed animals, while a decrease was observed in animals after aerosol exposure, resulting in a significant difference between aerosol and fomite exposed hamsters (N = 4, Kruskal-Wallis test, followed by Dunn's multiple comparisons test,  $p = 0.0286$ ). While not significant, a trend of decreased serum levels of interferon (INF)- $\gamma$  as compared to uninfected animals, was observed. No significant differences were seen for serum levels of interleukin (IL)-6.

Irrespective of exposure route, all exposed animals seroconverted at 14 DPI as seen by the presence of antibodies targeting the SARS-CoV-2 spike measured by ELISA (Fig 4 b). The magnitude of humoral response was linked to the exposure route. I.N. exposure resulted in the strongest, and significantly higher antibody response when compared to fomite exposure (N = 4, Kruskal-Wallis test, followed by Dunn's multiple comparisons test,  $p = 0.0209$ ). No significant difference was observed between I.N. and aerosol exposed animals. Taken together this suggests a predominantly anti-inflammatory immune response is mounted after fomite exposure, as compared to aerosol exposure, which may protect from more severe outcome, yet is also linked to a weaker, but still substantial, antibody response.

### **Viral shedding is exposure route dependent**

To gain an understanding of route-dependent virus shedding patterns of SARS-CoV-2 in the Syrian hamster, daily oropharyngeal and rectal swabs were taken until 7 DPI, after which swabs were taken thrice weekly (Fig 4 c, d). Oropharyngeal swabs are a measurement of respiratory shedding while rectal swabs assess intestinal shedding. Viral sgRNA, a marker of virus replication [27], was detected in both swabs from all exposed animals on at least one day. When comparing the overall respiratory shedding profile between the exposure routes, different

patterns were observed. I.N. inoculation resulted in high viral loads starting at 1 DPI and continued up until 6 DPI, before sgRNA levels started to decrease. In the aerosol inoculated group, the peak of virus shedding was reached on 2 DPI and viral sgRNA levels decreased immediately thereafter. In contrast, animals exposed through the fomite route demonstrated different shedding kinetics as compared to aerosol and I.N. groups with an increase in viral sgRNA shedding over multiple days, until peak shedding was reached at 5 DPI. While a trend seemed present for higher individual peak shedding in I.N. and fomite groups, no significant difference was detected (Fig 4 e;  $N = 4$ , Kruskal-Wallis test, followed by Dunn's multiple comparisons test,  $p = 0.8400$ ). In comparison, intestinal shedding demonstrated median lower viral loads with no significant difference between groups:  $N = 4$  Kruskal-Wallis test, followed by Dunn's multiple comparisons test,  $p = 0.1512$  (Fig 4 d, e). Looking at the shedding profile of individual animals across groups, intestinal shedding was observed for a maximum of three consecutive days with sgRNA only being detected in swabs for one or two consecutive days for most positive animals. To evaluate the overall shedding burden generated by each exposure route, the cumulative shedding up until 14 DPI (area under the curve (AUC)) was compared. Aerosol exposure led to overall less viral RNA in oropharyngeal swabs as compared to I.N. and fomite exposure ( $N = 4$ , Kruskal-Wallis test, followed by Dunn's multiple comparisons test,  $p = 0.0263$ ). In contrast, most commutative viral sgRNA was detected in rectal swabs of aerosol exposed animals (Fig 4 f). Taken together, these data suggest that severity of disease is not indicative of the duration and cumulative amount of virus shed after infection.

### **Early shedding profile may predict disease severity and corresponding immune response**

As we observed different impacts on disease profiles between exposure routes, we next investigated potential predictability of disease through early shedding patterns. Cytokine responses as a measurement of the immune status (4 DPI) were included in the correlations

between early shedding (2 DPI), peak shedding, peak weight loss, lung titers and pathology at 4 DPI (Fig 3 g). Lung viral titers were positively correlated significantly with the amount of viral RNA detected in oropharyngeal swabs at 2 DPI (Spearman correlation test,  $N = 12$ ,  $p = 0.047$ ). Lung titers showed a positive relationship with upper and lower respiratory tract pathology and weight loss. This suggests that early time point respiratory shedding (before disease manifestation) may predict the acute disease manifestation.

Serum levels of IL-4, IL-6 and IL-10 did not show any significant correlations with parameters of disease severity; however, a clear negative relationship could be seen in the correlations. TNF- $\alpha$ , negatively correlated to IL-4 and IL-10 levels (Spearman correlation test,  $N = 12$ ,  $p = 0.048$  and  $p = 0.049$ , respectively). A positive correlation between early rectal shedding and TNF- $\alpha$  serum levels and olfactory pathology was observed (Spearman correlation test,  $N = 12$ ,  $p = 0.0002$  and  $p = 0.001$ , respectively) (Fig 4g).

#### **Airborne transmission is more efficient than fomite transmission in the Syrian hamster**

To investigate viral fomite contamination of caging, daily swabs were taken from surfaces in cages containing one I.N. inoculated hamsters, up to 7 DPI (Sup Fig 1 b, c). Viral gRNA was detectable at 1 DPI in all samples, sgRNA was detectable for 7/8 (87.5%) bedding samples and 3/8 (37.5%) cage samples, and at 2 DPI in 8/8 cages for both samples. Viral sgRNA was detectable at high concentrations up until 7 DPI, with peak concentrations seen on 2 and 3 DPI, suggesting a robustly contaminated caging environment.

To assess the potential risk of fomite transmission, we introduced sentinel hamsters to cages after housing two I.N. infected animals for 4 days. (Fig 5 a). No signs of disease or weight loss were observed in sentinel animals, but seroconversion was seen in 4 out of 8 animals (Fig 5 f) at 21 days after exposure (DPE) to a contaminated cage, confirming that hamster-to-hamster indirect transmission via fomites can occur (Fig 5 h).

Next, the efficiency and dynamics of airborne hamster-to-hamster transmission were assessed. For this purpose, we designed a cage divider, which allowed airflow but no direct contact or fomite transmission between animals. (Fig 5 b, Fig 5 c, d, and supplemental video). We used a particle sizer to assess the effect of the cage divider on blocking particle flow. We observed that cross-over of smaller particles ( $<10\ \mu\text{m}$ ) was blocked approx. 60%, whilst larger particles ( $>10\ \mu\text{m}$ ), were reduced over 85% on the sentinel side (Fig 5 d, e).

In the first experiment, one sentinel hamster was placed on the side of the divider downflow from one infected animal ( $N = 8$ ). In contrast to animals exposed directly to aerosolized virus, no signs of disease or weight loss were observed in any of the sentinel animals (Fig 5 g). However, all animals seroconverted. To assess the importance of directional airflow, airborne transmission was also modeled for 4 transmission pairs housing the sentinel against the airflow (Fig 5 b, c). Only one out of 4 of the sentinels placed against airflow seroconverted (Fig 5 g), suggesting, as expected, that directional airflow is key to airborne transmission. When comparing the antibody response at 21 DPI/DPE, no significant difference was determined between the donor I.N. inoculated animals and those that seroconverted after airborne transmission (100%), while titers for animals that seroconverted after fomite transmission (50%) were lower (Fig 5 g, Kruskal-Wallis test, followed by Dunn's multiple comparisons test,  $N = 8$  and  $N = 4$ ,  $p = >0.9999$  and  $p = 0.2488$ , respectively). Titers were comparable to those observed after direct inoculation. Together, this suggests that hamster-to-hamster airborne transmission may present with asymptomatic disease manifestation, yet the humoral immune memory is comparably robust.

To investigate the transmission risk posed by animals after fomite or airborne transmission, the respiratory shedding profile was determined. Viral shedding was demonstrated in 4 out of 8



sentinel hamsters after exposure to contaminated cages on multiple consecutive days. Shedding was observed at 1 DPE, with peak viral sgRNA being seen at 4/5 DPE, like what was observed in hamsters directly exposed to fomites (Fig 4 c). For airborne transmission, sentinels downstream of airflow started shedding by 1 DPE, and all 8 animals had high amounts of viral sgRNA in the oropharyngeal cavity by 2 DPE, which remained high until 6 DPE. This data suggest that this indirect exposure route presents with a distinctly different disease manifestation and shedding profile than direct aerosol exposure (Fig 5 i). Of note, commutative viral shedding between infected airborne exposed animals showed no difference to those infected through fomite transmission (Fig 5 j). These data imply that, whilst presenting with no or very mild disease phenotypes, both routes of indirect exposure between animals create a mimicry of asymptomatic carriers.

## Discussion

SARS-CoV-2 transmission is driven by close proximity, confined environment, and the frequency of contacts [28]. Infection with SARS-CoV-2 is believed to be driven by direct contact, inhalation of virus within respiratory droplet nuclei, contact with droplet contaminated surfaces or any combination between these exposures. Yet, the relative contribution of each of the potential routes of exposure in relationship to human-to-human transmission has been elusive. Moreover, the relationship between exposure route and the differential impact on disease severity has been equally obscure. Animal models are essential to model experimental transmission under controlled conditions, as transmission involves several factors: duration and magnitude of virus shedding, stability of the virus in aerosols or on surfaces, and the subsequent infection of another host.

Our data indicate that in addition to the exposure dose [29] and underlying host conditions [30], disease is a function of exposure route. The Syrian hamster model recapitulates several

aspects of COVID-19, including upper and lower respiratory tract pathology, SARS-CoV-2 shedding and potential transmission between animals [24-26, 29, 31-33]. Typically, experimental studies with SARS-CoV-2 in hamsters rely on intranasal inoculation. This route of inoculation establishes robust infection but does not resemble natural infection via aerosols or respiratory droplets. Here we directly compared natural transmission routes, designed to mimic airborne and fomite exposure. The initial respiratory tropism of SARS-CoV-2 was determined by the exposure route, aerosol exposure deposited SARS-CoV-2 more efficiently in both the upper and lower respiratory tract. As a result, the SARS-CoV-2 replication kinetics displayed higher viral titers in trachea and lung early in the infection compared to the I.N. inoculated animals. Despite a 10-fold lower inoculation dose, exposing Syrian hamsters to aerosolized SARS-CoV-2 resulted in more rapid virus replication in the lung and weight loss compared to I.N. inoculation. In contrast, fomite inoculation displayed a delayed disease manifestation with a prolonged time between exposure and viral replication in the lung leading to reduced disease severity. This delay suggests that for fomite infection viral replication may occur in the oropharynx before being inhaled [32]. It's possible that this may give time for a regulating immune response characterized by a systemic lack of TNF- $\alpha$  and an increased IL-4 and IL-10 presence demonstrated in this work. This in turn may reduce immune pathology in the lung even with the observed viral titers at 4 DPI not being significantly lower as compared to aerosol inoculation.

No human data is currently available on the influence of transmission route on COVID-19 severity. In experimental Nipah virus infection studies in non-human primates, particle size directly influenced the disease manifestations. Aerosol exposure led to a rapidly progressing respiratory disease whereas large droplet exposure led to an extended disease course that does not have the prominent respiratory features [34, 35]. These findings suggest more severe disease is associated with direct deposition of the virus in the lower respiratory tract, whereas with milder disease the first viral replication occurs in upper respiratory tract. This further implies

that besides lowering viral dose, intervention measures such as face-coverings may also serve to minimize disease by limiting the deposition of viral particles into the lower respiratory tract [36-38]. More investigations are required to validate if this occurs [39].

Our data reflects findings in humans, where no clear correlation could be drawn between severity of disease and shedding time. The aerosol exposed animals shed cumulatively less virus, while fomite exposure resulted in equally high peak viral shedding compared to I.N. inoculated animals. In humans, serological analyses suggest that approximately 17% of infections remain mild to asymptomatic [40]. There is evidence of both asymptomatic and symptomatic shedding [41-44], suggesting that mild or asymptomatic disease contribute the same transmission risk as more severe COVID-19 cases [45, 46]. Asymptomatic disease in humans may present with lower shedding dose or faster decline [5], which we did not observe in this animal model.

The relative contribution of fomite and airborne transmission to the spread of SARS-CoV-2 is still disputed [47]. The risk of fomite transmission was previously assessed as lower compared to airborne transmission in a limited study in the Syrian hamster. Fomite transmission occurred in only 1 of 3 sentinels placed into contaminated cages at viral RNA peak contamination [25]. Surprisingly, we demonstrate here that fomite transmission may still occur (4 out of 8) when peak shedding of infectious virus has waned as previously shown [25], and environmental contamination is expected to be reduced. Importantly, this implies that even with an increased understanding of airborne transmission involvement at this stage of the pandemic, the risk of fomite transmission in humans should not be underestimated. In particular, fomite transmission may be more likely to occur in nosocomial settings that present a combination of fomite and aerosol generating procedures and may potentially be further enhanced with more susceptible hospital population [48, 49].

Within our transmission set-up we show a selective reduction of largest particles ( $>10\ \mu\text{m}$ ), but that this exclusion was not absolute (Fig 5). Therefore, we cannot formally distinguish between true aerosol transmission (droplet nuclei  $< 5\ \mu\text{m}$ ), droplet transmission ( $> 10\ \mu\text{m}$ ), or a combination of these two. Previous studies have shown that SARS-CoV-2 can be transmitted through the air in a ferret model over short and moderate distance [50, 51] and in hamsters over short distance [25, 52]. In our study we were able to show a high efficiency of airborne transmission with 100% of the sentinels becoming infected. When reversing the airflow from uninfected animals toward infected animals, a sharp reduction in transmission was observed. This suggest that directional airflow plays an important role in the transmission of SARS-CoV-2. This has also been observed in human-to-human transmission events, where transmission in confined spaces (e.g. restaurant) was directed by airflow [16, 53, 54]. Control measures focused on strategically designed room ventilation will directly aid the control of the pandemic [55, 56].

In this study, we showed the relative contribution of airborne and fomite transmission and the impact of exposure route on disease. The hamster transmission model will be crucial to assess the transmission and pathogenic potential of novel SARS-CoV-2 strains, in the light of the continuing SARS-CoV-2 virus evolution [57]. In addition, this work will allow the development of effective public health countermeasures aimed at blocking human-to-human transmission. The findings of this study suggest that using more natural routes of transmission are highly suitable for accurately assessing the transmission potential and pathogenicity of novel evolved strains [57]. Additionally, these data strongly suggest that the Syrian hamster model would be very suitable to investigate the true limits of airborne transmission and applying this to prevention studies as has been previously demonstrated for short distance airborne transmission with masks [52]. Furthermore, demonstrating hamster-to-hamster natural transmission via different routes indicates that this model is useful for setting up complex intervention experiments involving different transmission routes.

## Materials and Methods

### *Ethics statement*

Approval of animal experiments was obtained from the Institutional Animal Care and Use Committee of the Rocky Mountain Laboratories. Performance of experiments was done following the guidelines and basic principles in the United States Public Health Service Policy on Humane Care and Use of Laboratory Animals and the Guide for the Care and Use of Laboratory Animals. Work with infectious SARS-CoV-2 strains under BSL3 conditions was approved by the Institutional Biosafety Committee (IBC). Inactivation and removal of samples from high containment was performed per IBC-approved standard operating procedures.

### *Virus and cells*

SARS-CoV-2 strain nCoV-WA1-2020 (MN985325.1) was provided by CDC, Atlanta, USA. Virus propagation was performed in VeroE6 cells in Dulbecco's Modified Eagle Medium (DMEM) supplemented with 2% foetal bovine serum (FBS), 2 mM L-glutamine, 100 U/mL penicillin and 100 µg/mL streptomycin. Cells were cultured in DMEM supplemented with 10% FBS, 2 mM L-glutamine, 100 U/mL penicillin and 100 µg/mL streptomycin. No contaminants were detected; the used virus was 100% identical to the initial deposited GenBank sequence (MN985325.1).

### *Inoculation experiments*

Four to six-week-old female Syrian hamsters (ENVIGO) were inoculated (12 animals per route) either intranasally (I.N.), via aerosol exposure or via exposure to a fomite. Hamsters were housed in groups of 4 animals. I.N. inoculation was performed with 40 µL sterile DMEM containing  $8 \times 10^4$  TCID<sub>50</sub> SARS-CoV-2. For exposure through aerosols animals were subjected to  $1.5 \times 10^3$  TCID<sub>50</sub> SARS-CoV-2 during a 10 min exposure time. Aerosol inoculation using the AeroMP aerosol management platform (Biaera technologies, USA) was performed as described

previously [58]. Briefly, non-anesthetized hamsters were exposed to a single exposure whilst contained in a stainless-steel wire mesh cage. Aerosol droplet nuclei were generated by a 3-jet collision nebulizer (Biaera technologies, USA) and ranged from 1-5  $\mu\text{m}$  in size. Respiratory minute volume rates of the animals were determined using the methods of Alexander *et al.* [59]. Weights of the animals were averaged and the estimated inhaled dose was calculated using the simplified formula  $D = R \times C_{\text{aero}} \times T_{\text{exp}}$  [60], where  $D$  is the inhaled dose,  $R$  is the respiratory minute volume (L/min),  $C_{\text{aero}}$  is the aerosol concentration ( $\text{TCID}_{50}/\text{L}$ ), and  $T_{\text{exp}}$  is duration of the exposure (min). Fomite exposure was conducted by placing a polypropylene dish into the cage containing 40  $\mu\text{L}$  of  $8 \times 10^4$   $\text{TCID}_{50}$  SARS-CoV-2 per hamster (total dose per cage:  $3.2 \times 10^5$   $\text{TCID}_{50}$ ).

At 1- and 4-days post infection (DPI), four hamsters for each route were euthanized, and tissues were collected. The remaining 4 animals for each route were euthanized at 14 DPI for disease course assessment and shedding analysis. Hamsters were weighted daily, and oropharyngeal and rectal swabs were taken daily until day 7 and then thrice a week. Swabs were collected in 1 mL DMEM with 200 U/mL penicillin and 200  $\mu\text{g}/\text{mL}$  streptomycin. Hamsters were observed daily for clinical signs of disease.

#### *Airborne Transmission experiments*

Airborne transmission was examined by co-housing hamsters (1:1) in specially designed cages with a perforated plastic divider dividing the living space in half. This divider prevented direct contact between the donor/primary infected and sentinel hamster and the movement of bedding material. Regular bedding was replaced by alpha-dri bedding to avoid the generation of dust particles. Donor hamsters were infected intranasally as described above and sentinel hamsters placed on the other side of a divider afterwards. Hamsters were followed as described above until 21 DPI. Experiments were performed with cages placed into a standard rodent cage rack,

under normal airflow conditions (Fig 5 c, d, e). Sentinels were either placed in the direction of the airflow, or against it (Fig 5 b).

#### *Fomite Transmission experiments*

Fomite transmission was examined by infecting donor hamsters as described above by I.N. inoculation. Two animals per cage were housed for 4 days. Regular bedding was replaced by alpha-dri bedding to avoid the generation of dust particles. At 4 DPI, donors were euthanized, and sentinel animals (2 animals per cage) were placed into the contaminated cage (Fig 5 a). Hamsters were followed as described above until DPI 21; bedding and cages were left undisturbed.

#### *Particle sizing*

Transmission cages were modified by introducing an inlet on the side of the infected hamster side, and sample ports on each end of the cage for measurement of particles in the air under constant airflow condition. Particles were generated by spraying a 20% (v/v) glycerol solution with a standard spray bottle through the cage inlet. The particle size range of the generated particles was measured using a Model 3321 aerodynamic particle sizer spectrometer (TSI). The cage was coated with two sprays at an interval of 30 seconds (s) and after a third spray the sample port was opened, and a sample was analyzed. The cage was sprayed every 30 s and five samples were analysed (5 runs, each 60 s) for both donor side (primary infected side) and sentinel side.

#### *Histopathology and immunohistochemistry*

Necropsies and tissue sampling were performed according to IBC-approved protocols. Tissues were fixed for a minimum of 7 days in 10% neutral buffered formalin with 2 changes. Tissues were placed in cassettes and processed with a Sakura VIP-6 Tissue Tek, on a 12-hour automated schedule, using a graded series of ethanol, xylene, and ParaPlast Extra. Prior to staining, embedded tissues were sectioned at 5  $\mu$ m and dried overnight at 42°C. Using GenScript U864YFA140-4/CB2093 NP-1 (1:1000) specific anti-CoV immunoreactivity was detected using the Vector Laboratories ImPress VR anti-rabbit IgG polymer (# MP-6401) as secondary antibody. The tissues were then processed using the Discovery Ultra automated processor (Ventana Medical Systems) with a ChromoMap DAB kit Roche Tissue Diagnostics (#760-159).

#### *Viral RNA detection*

Swabs from hamsters were collected as described above. Cage and bedding material were sampled with prewetted swabs in 1 mL of DMEM supplemented with 200 U/mL penicillin and 200  $\mu$ g/mL streptomycin. Then, 140  $\mu$ L was utilized for RNA extraction using the QIAamp Viral RNA Kit (Qiagen) using QIAcube HT automated system (Qiagen) according to the manufacturer's instructions with an elution volume of 150  $\mu$ L. Sub-genomic (sg) viral RNA and genomic (g) was detected by qRT-PCR [27, 61]. Five  $\mu$ L RNA was tested with TaqMan™ Fast Virus One-Step Master Mix (Applied Biosystems) using QuantStudio 6 Flex Real-Time PCR System (Applied Biosystems) according to instructions of the manufacturer. Ten-fold dilutions of SARS-CoV-2 standards with known copy numbers were used to construct a standard curve and calculate copy numbers/mL.

#### *Viral titration*

Viable virus in tissue samples was determined as previously described [62]. In brief, lung, trachea, brain, and gastrointestinal tissue samples were weighted, then homogenized in 1 mL of



DMEM (2% FBS). VeroE6 cells were inoculated with ten-fold serial dilutions of tissue homogenate, incubated 1 h at 37°C, the first two dilutions washed twice with 2% DMEM. Cells were incubated with tissue homogenate for 6 days, then scored for cytopathic effect. TCID<sub>50</sub>/mL was calculated by the method of Spearman-Kärber and adjusted for tissue weight.

### *Serology*

Serum samples were inactivated with γ-irradiation (2 mRad) and analyzed as previously described [63]. In brief, maxisorp plates (Nunc) were coated with 50 ng spike protein (generated in-house) per well and incubated overnight at 4°C. After blocking with casein in phosphate buffered saline (PBS) (ThermoFisher) for 1 h at room temperature (RT), serially diluted 2-fold serum samples (duplicate, in blocking buffer) were incubated for 1 h at RT. Spike-specific antibodies were detected with goat anti-hamster IgG Fc (horseradish peroxidase (HRP)-conjugated, Abcam) for 1 h at RT and visualized with KPL TMB 2-component peroxidase substrate kit (SeraCare, 5120-0047). The reaction was stopped with KPL stop solution (Seracare) and read at 450 nm. Plates were washed 3 to 5 x with PBS-T (0.1% Tween) for each wash. The threshold for positivity was calculated as the average plus 3 x the standard deviation of negative control hamster sera.

### *Cytokine analysis*

Cytokine concentrations were determined using a commercial hamster ELISA kit for TNF-α, INF-γ, IL-6, IL-4, and IL-10 available at antibodies.com, according to the manufacturer's instructions (antibodies.com; A74292, A74590, A74291, A74027, A75096). Samples were pre-diluted 1:50.

### *Statistical Analysis*

Heatmaps and correlation graphs were made in R [64] using pheatmap [65] and corrplot [66] packages. Significance test were performed as indicated where appropriate: Spearman correlation test, two-way ANOVA and Kruskal-Wallis test. Statistical significance levels were determined as follows: ns =  $p > 0.05$ ; \* =  $p \leq 0.05$ ; \*\* =  $p \leq 0.01$ ; \*\*\* =  $p \leq 0.001$ ; \*\*\*\* =  $p \leq 0.0001$ .

## Acknowledgements

The authors would like to thank the Rocky Mountain Veterinary branch, including Nicki Arndt, Amanda Weidow and Brian Mosbrucker for assistance with high containment husbandry and cage design and testing, Greg Saturday for assistance with necropsy, Tina Thomas for assistance with histology, Stephanie Seifert for assistance in study protocol editing, and Rose Perry and Ryan Kissinger for assistance with the figures. This research was supported by the Intramural Research Program of the National Institute of Allergy and Infectious Diseases (NIAID), National Institutes of Health (NIH).

## Disclosure statement

The authors declare no competing financial interests.

## References

1. WHO, *Coronavirus disease 2019 (COVID-19) Situation Report – 52*. 2020.
2. Nie, S., et al., *Coronavirus Disease 2019-related dyspnea cases difficult to interpret using chest computed tomography*. Respiratory medicine, 2020. **167**: p. 105951-105951.
3. Parry, A.H., et al., *Spectrum of chest computed tomographic (CT) findings in coronavirus disease-19 (COVID-19) patients in India*. European Journal of Radiology, 2020. **129**: p. 109147-109147.
4. van Kampen, J.J.A., et al., *Shedding of infectious virus in hospitalized patients with coronavirus disease-2019 (COVID-19): duration and key determinants*. medRxiv, 2020: p. 2020.06.08.20125310.
5. Cevik, M., et al., *SARS-CoV-2, SARS-CoV, and MERS-CoV viral load dynamics, duration of viral shedding, and infectiousness: a systematic review and meta-analysis*. The Lancet Microbe, 2020.

6. Organization, W.H., *Transmission of SARS-CoV-2: implications for infection prevention precautions*. 2020.
7. van Doremalen, N., et al., *Aerosol and Surface Stability of SARS-CoV-2 as Compared with SARS-CoV-1*. *N Engl J Med*, 2020. **382**(16): p. 1564-1567.
8. Chia, P.Y., et al., *Detection of air and surface contamination by SARS-CoV-2 in hospital rooms of infected patients*. *Nat Commun*, 2020. **11**(1): p. 2800.
9. Guo, Z.D., et al., *Aerosol and Surface Distribution of Severe Acute Respiratory Syndrome Coronavirus 2 in Hospital Wards, Wuhan, China, 2020*. *Emerg Infect Dis*, 2020. **26**(7): p. 1583-1591.
10. Zhou, J., et al., *Investigating SARS-CoV-2 surface and air contamination in an acute healthcare setting during the peak of the COVID-19 pandemic in London*. *medRxiv*, 2020: p. 2020.05.24.20110346.
11. Pastorino, B., et al., *Prolonged Infectivity of SARS-CoV-2 in Fomites*. *Emerg Infect Dis*, 2020. **26**(9): p. 2256-7.
12. Matson, M.J., et al., *Effect of Environmental Conditions on SARS-CoV-2 Stability in Human Nasal Mucus and Sputum*. *Emerg Infect Dis*, 2020. **26**(9): p. 2276-8.
13. Bohannon, J.K., et al., *Generation and characterization of large-particle aerosols using a center flow tangential aerosol generator with a non-human-primate, head-only aerosol chamber*. *Inhal Toxicol*, 2015. **27**(5): p. 247-53.
14. Cheng, V.C., et al., *Air and environmental sampling for SARS-CoV-2 around hospitalized patients with coronavirus disease 2019 (COVID-19)*. *Infect Control Hosp Epidemiol*, 2020. **41**(11): p. 1258-1265.
15. Liu, Y., et al., *Aerodynamic analysis of SARS-CoV-2 in two Wuhan hospitals*. *Nature*, 2020. **582**(7813): p. 557-560.
16. Lu, J., et al., *COVID-19 Outbreak Associated with Air Conditioning in Restaurant, Guangzhou, China, 2020*. *Emerg Infect Dis*, 2020. **26**(7): p. 1628-1631.
17. Ma, J., et al., *Exhaled breath is a significant source of SARS-CoV-2 emission*. *medRxiv*, 2020: p. 2020.05.31.20115154.
18. Miller, S.L., et al., *Transmission of SARS-CoV-2 by inhalation of respiratory aerosol in the Skagit Valley Chorale superspreading event*. *Indoor Air*, 2020.
19. National Academies of Sciences, E. and Medicine, *Airborne Transmission of SARS-CoV-2: Proceedings of a Workshop—in Brief*, ed. M. Shelton-Davenport, et al. 2020, Washington, DC: The National Academies Press. 18.
20. Santarpia, J.L., et al., *Aerosol and Surface Transmission Potential of SARS-CoV-2*. *medRxiv*, 2020: p. 2020.03.23.20039446.

21. Lednicky, J.A., et al., *Viable SARS-CoV-2 in the air of a hospital room with COVID-19 patients*. International Journal of Infectious Diseases, 2020. **100**: p. 476-482.
22. Santarpia, J.L., et al., *Aerosol and surface contamination of SARS-CoV-2 observed in quarantine and isolation care*. Scientific Reports, 2020. **10**(1): p. 12732.
23. Colaneri, M., et al., *Severe acute respiratory syndrome coronavirus 2 RNA contamination of inanimate surfaces and virus viability in a health care emergency unit*. Clinical Microbiology and Infection, 2020. **26**(8): p. 1094.e1-1094.e5.
24. Rosenke, K., et al., *Defining the Syrian hamster as a highly susceptible preclinical model for SARS-CoV-2 infection*. Emerg Microbes Infect, 2020: p. 1-36.
25. Sia, S.F., et al., *Pathogenesis and transmission of SARS-CoV-2 in golden hamsters*. Nature, 2020.
26. Chan, J.F.-W., et al., *Simulation of the Clinical and Pathological Manifestations of Coronavirus Disease 2019 (COVID-19) in a Golden Syrian Hamster Model: Implications for Disease Pathogenesis and Transmissibility*. Clinical Infectious Diseases, 2020.
27. Corman, V.M., et al., *Detection of 2019 novel coronavirus (2019-nCoV) by real-time RT-PCR*. Euro Surveill, 2020. **25**(3).
28. Sun, K., et al., *Transmission heterogeneities, kinetics, and controllability of SARS-CoV-2*. Science, 2020.
29. Muñoz-Fontela, C., et al., *Animal models for COVID-19*. Nature, 2020. **586**(7830): p. 509-515.
30. Guan, W.J., et al., *Comorbidity and its impact on 1590 patients with COVID-19 in China: a nationwide analysis*. Eur Respir J, 2020. **55**(5).
31. Bryche, B., et al., *Massive transient damage of the olfactory epithelium associated with infection of sustentacular cells by SARS-CoV-2 in golden Syrian hamsters*. Brain Behav Immun, 2020.
32. Chak-Yiu Lee, A., et al., *Oral SARS-CoV-2 inoculation establishes subclinical respiratory infection with virus shedding in golden Syrian hamsters*. Cell Rep Med, 2020: p. 100121.
33. Osterrieder, N., et al., *Age-Dependent Progression of SARS-CoV-2 Infection in Syrian Hamsters*. Viruses, 2020. **12**(7).
34. Hammoud, D.A., et al., *Aerosol exposure to intermediate size Nipah virus particles induces neurological disease in African green monkeys*. PLOS Neglected Tropical Diseases, 2018. **12**(11): p. e0006978.
35. Lee, J.H., et al., *The Use of Large-Particle Aerosol Exposure to Nipah Virus to Mimic Human Neurological Disease Manifestations in the African Green Monkey*. The Journal of Infectious Diseases, 2019. **221**(Supplement\_4): p. S419-S430.
36. Leung, N.H.L., et al., *Respiratory virus shedding in exhaled breath and efficacy of face masks*. Nature Medicine, 2020. **26**(5): p. 676-680.

37. Konda, A., et al., *Aerosol Filtration Efficiency of Common Fabrics Used in Respiratory Cloth Masks*. ACS Nano, 2020. **14**(5): p. 6339-6347.
38. Kähler, C.J. and R. Hain, *Fundamental protective mechanisms of face masks against droplet infections*. J Aerosol Sci, 2020. **148**: p. 105617.
39. Gandhi, M. and G.W. Rutherford, *Facial Masking for Covid-19 — Potential for “Variolation” as We Await a Vaccine*. New England Journal of Medicine, 2020. **383**(18): p. e101.
40. Byambasuren, O., et al., *Estimating the extent of asymptomatic COVID-19 and its potential for community transmission: Systematic review and meta-analysis*. Official Journal of the Association of Medical Microbiology and Infectious Disease Canada, 2020. **COVID-19**: p. Accepted version, e20200030.
41. He, G., et al., *The clinical feature of silent infections of novel coronavirus infection (COVID-19) in Wenzhou*. Journal of Medical Virology, 2020. **92**(10): p. 1761-1763.
42. Rothe, C., et al., *Transmission of 2019-nCoV Infection from an Asymptomatic Contact in Germany*. N Engl J Med, 2020. **382**(10): p. 970-971.
43. Meng, H., et al., *CT imaging and clinical course of asymptomatic cases with COVID-19 pneumonia at admission in Wuhan, China*. Journal of Infection, 2020. **81**(1): p. e33-e39.
44. Mizumoto, K., et al., *Estimating the asymptomatic proportion of coronavirus disease 2019 (COVID-19) cases on board the Diamond Princess cruise ship, Yokohama, Japan, 2020*. Eurosurveillance, 2020. **25**(10): p. 2000180.
45. Bai, Y., et al., *Presumed Asymptomatic Carrier Transmission of COVID-19*. JAMA, 2020. **323**(14): p. 1406-1407.
46. Bae, S.H., et al., *Asymptomatic Transmission of SARS-CoV-2 on Evacuation Flight*. Emerging Infectious Disease journal, 2020. **26**(11): p. 2705.
47. Goldman, E., *Exaggerated risk of transmission of COVID-19 by fomites*. Lancet Infect Dis, 2020. **20**(8): p. 892-893.
48. Judson, S.D. and V.J. Munster, *A framework for nosocomial transmission of emerging coronaviruses*. Infect Control Hosp Epidemiol, 2020: p. 1-2.
49. Judson, S.D. and V.J. Munster, *Nosocomial Transmission of Emerging Viruses via Aerosol-Generating Medical Procedures*. Viruses, 2019. **11**(10).
50. Kutter, J.S., et al., *SARS-CoV and SARS-CoV-2 are transmitted through the air between ferrets over more than one meter distance*. bioRxiv, 2020: p. 2020.10.19.345363.
51. Richard, M., et al., *SARS-CoV-2 is transmitted via contact and via the air between ferrets*. Nat Commun, 2020. **11**(1): p. 3496.

52. Chan, J.F., et al., *Surgical mask partition reduces the risk of non-contact transmission in a golden Syrian hamster model for Coronavirus Disease 2019 (COVID-19)*. Clin Infect Dis, 2020.
53. Hamner, L., et al., *High SARS-CoV-2 Attack Rate Following Exposure at a Choir Practice - Skagit County, Washington, March 2020*. MMWR. Morbidity and mortality weekly report, 2020. **69**(19): p. 606-610.
54. Leclerc, Q.J., et al., *What settings have been linked to SARS-CoV-2 transmission clusters?* : Wellcome Open Res. 2020 Jun 5;5:83. doi: 10.12688/wellcomeopenres.15889.2. eCollection 2020.
55. Morawska, L., et al., *How can airborne transmission of COVID-19 indoors be minimised?* Environment international, 2020. **142**: p. 105832-105832.
56. CDC, *Ventilation*. 2020.
57. Hou, Y.J., et al., *SARS-CoV-2 D614G variant exhibits efficient replication ex vivo and transmission in vivo*. Science, 2020.
58. de Wit, E., et al., *The Middle East respiratory syndrome coronavirus (MERS-CoV) does not replicate in Syrian hamsters*. PLoS One, 2013. **8**(7): p. e69127.
59. Alexander, D.J., et al., *Association of Inhalation Toxicologists (AIT) working party recommendation for standard delivered dose calculation and expression in non-clinical aerosol inhalation toxicology studies with pharmaceuticals*. Inhal Toxicol, 2008. **20**(13): p. 1179-89.
60. Hartings, J.M. and C.J. Roy, *The automated bioaerosol exposure system: preclinical platform development and a respiratory dosimetry application with nonhuman primates*. J Pharmacol Toxicol Methods, 2004. **49**(1): p. 39-55.
61. Corman, V.M., et al., *Detection of 2019 novel coronavirus (2019-nCoV) by real-time RT-PCR*. Euro surveillance : bulletin European sur les maladies transmissibles = European communicable disease bulletin, 2020. **25**(3): p. 2000045.
62. van Doremalen, N., et al., *Efficacy of antibody-based therapies against Middle East respiratory syndrome coronavirus (MERS-CoV) in common marmosets*. Antiviral Res, 2017. **143**: p. 30-37.
63. Yinda, C.K., et al., *K18-hACE2 mice develop respiratory disease resembling severe COVID-19*. bioRxiv, 2020.
64. R Development Core Team, *R: A language and Environment for Statistical computing* 2010, R Foundation for Statistical Computing.
65. Kolde, R., *Implementation of heatmaps that offers more control over dimensions and appearance*. 2019.
66. Wei, T. and V. Simko, *R package "corrplot": Visualization of a Correlation Matrix*. 2017.



## Figure Legends

**Figure 1. Disease severity in Syrian hamsters.** **a.** Experimental layout for intranasal (I.N.), fomite and aerosol exposure experiments. White circle: inoculation, black: necropsy, grey, swab time-points **b.** Relative weight loss in hamsters after SARS-CoV-2 inoculation over time (DPI = day post inoculation,  $n = 4$  per group). The lines represent mean  $\pm$  SEM. Black line indicates weights of unexposed control group. Dotted vertical line represent averaged peak weight loss post inoculation or exposure. Statistical significance was measured using a Mann–Whitney two-sided test, p-values are shown. **c.** Violin plot with individuals and median of weight gain at 14 DPI. Statistical significance was measured using a Kruskal-Wallis test, followed by Dunn’s multiple comparison test. **d.** Violin plot with individual and median titers of infectious SARS-CoV-2 in the respiratory and intestinal tissues at 1 DPI and **e.** 4 DPI, Red: I.N, blue: aerosol, purple: fomite, black: unexposed; dotted horizontal line = limit of detection (0.5). GI = gastrointestinal tract;  $n = 4$  per group. Statistical significance was measured using a two-way ANOVA, followed by Tukey’s multiple comparison test. \* $P < 0.05$ , \*\* $P < 0.001$ , \*\*\* $P < 0.0001$ , \*\*\*\* $P < 0.0001$ . NS, not significant.

## Figure 2. Comparison of early replication of SARS-CoV-2 in respiratory tract

Comparison of replication of SARS-CoV-2 for intranasal (I.N.), aerosol and fomite inoculated hamsters at 1 day post inoculation (DPI) by immunohistochemistry **a, b, c.** SARS-CoV-2 antigen detection in ciliated epithelial cells of the nasal mucosa (200x). **d.** Nasal mucosa from a control hamster (200x). **e, f, g.** SARS-CoV-2 antigen detection throughout tracheal ciliated epithelial cells (400x). **h.** Normal tracheal mucosa from a control hamster. **i.** SARS-CoV-2 antigen detection focused on terminal bronchioles and adjacent alveolar spaces (100x). **j.** Lack of SARS-CoV-2 in epithelial cells with strong antigen detection noted in pulmonary macrophages (inset) (100x). **k.** Lack of SARS-CoV-2 antigen detection throughout the lung (100x). **l.** Normal lung from control hamster (100x). **m.** Quantitative comparison of antigen detection for lung (type I and type II pneumocytes, macrophages (mos), mucosa of the trachea and skull sections (olfactory and ciliated epithelium of the nasal turbinates) at 1 day post inoculation for I.N., aerosol, fomite, and control groups.

## Figure 3: Comparison of the respiratory tract pathology of SARS-CoV-2 Infected hamsters

Comparison of SARS-CoV-2 pathology for intranasal (I.N.), aerosol and fomite inoculated hamsters at 4 day post inoculation (DPI) **a.** Infiltration and disruption of the ciliated nasal mucosa by moderate numbers of leukocytes with multifocal epithelial cell necrosis (200x). **b.** Multifocal disruption of the nasal ciliated mucosa by low numbers of leukocytes with accumulations of degenerate leukocytes in the nasal passage (200x). **c.** Intact ciliated nasal mucosa with normal mucus presence within the lumen (200x). **d.** A control nasal turbinate with intact ciliated nasal mucosa and mucus within the lumen (200x). **e.** Disruption of the tracheal mucosa with single cell necrosis and infiltration by low numbers of leukocytes (400x). **f.** Unaffected tracheal mucosa (400x). **g.** Unaffected tracheal mucosa (400x). **h.** Section of tracheal mucosa from a control hamster (400x). **i-l.** No significant histopathologic lesions in the lung of any inoculation route at 1 day-post-inoculation (100x). **m.** Multifocal disruption of ciliated nasal mucosa with accumulation of cellular debris and degenerate leukocytes within the nasal passage (200x). **n.** Severe disruption and multifocal erosion of the nasal mucosa with accumulation of numerous degenerate leukocytes and abundant cellular debris within the nasal passage (200x). **o.** Ciliated epithelial cell degeneration and mucosal erosion with leukocyte infiltration into the lamina propria (200x). **p.** Normal nasal turbinate from a control hamster (200x). **q.** Focal disruption of the tracheal mucosa by low numbers of leukocytes (400x). **r.** Multifocal infiltration of the mucosa by moderate numbers of leukocytes and multifocal epithelial cell necrosis (400x). **s.** Multifocal loss of epithelial cilia and infiltration of the lamina propria by moderate numbers of leukocytes (400x). **t.** Normal tracheal mucosa from a control hamster (400x). **u.** Widespread, moderate to severe broncho-interstitial pneumonia (100x). **v.** Multifocal moderate broncho-interstitial pneumonia focused on terminal bronchioles (100x). **w.** Multifocal, mild interstitial pneumonia focused on terminal bronchioles (100x). **x.** Normal lung from a control hamster (100x). **y,z.** Clustering (Euclidean, complete) of animals based in viral titers in lung and trachea and quantitative assessment of pathology in the upper and lower respiratory tract on 1 DPI and 4 DPI. Heatmap colors refer to color scale on the right, grey = NA. Exposure route is indicated by color bar at the top.

**Figure 4. Exposure dependent SARS-CoV-2 acute systemic cytokine response, strength of humoral response and viral shedding profile.** **a.** Violin plots with individuals and median of serum concentrations of key cytokines (interferon (IFN)- $\gamma$ , tumour necrosis factor (TNF)- $\alpha$ , interleukin (IL)-6, IL-4, and IL-10) on 4 days post inoculation (DPI). **b.** Violin plots with individuals and median of endpoint IgG antibody titres against SARS-CoV-2 spike ectodomain measured by ELISA in serum. ELISAs were done once. **c.** Respiratory and **d.** intestinal viral

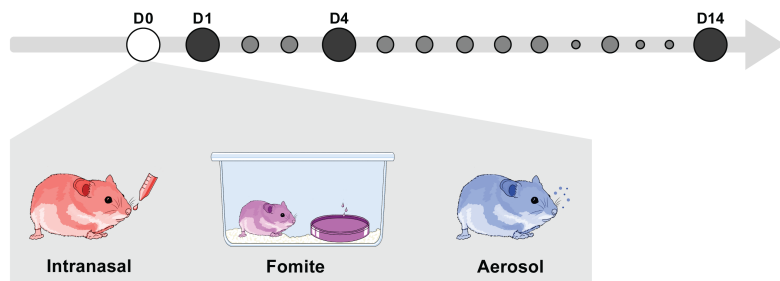
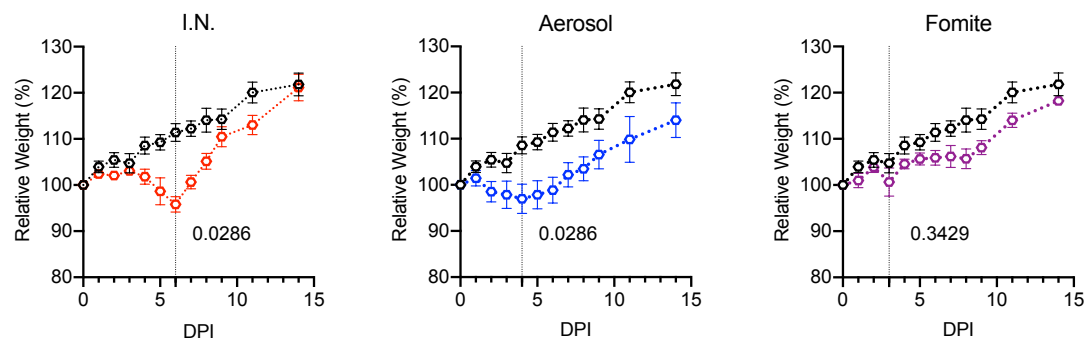
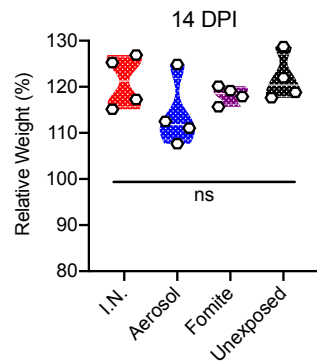
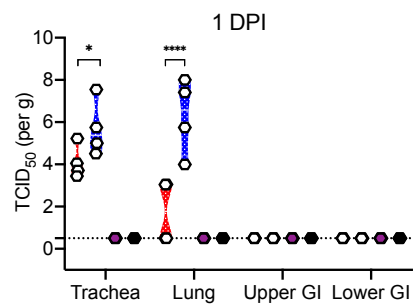
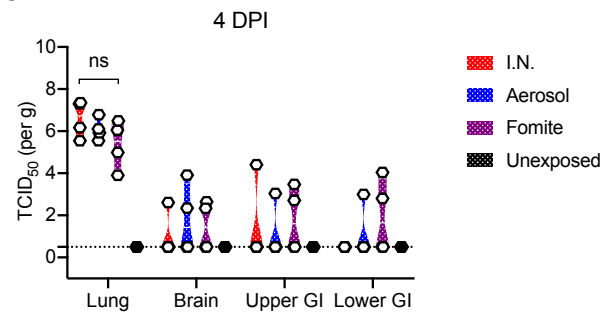


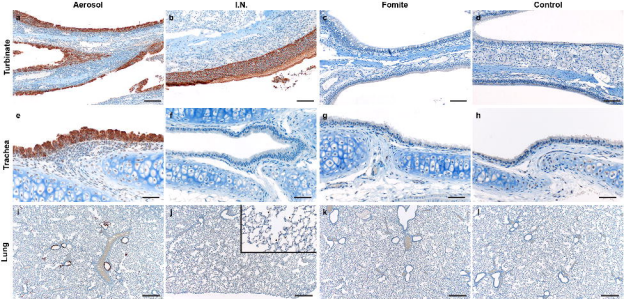
shedding of I.N., aerosol and fomite exposed hamsters. Median, 95% CI and individuals are shown. **e.** Peak shedding and **f.** cumulative (area under the curve (AUC) analysis) respiratory and intestinal shedding of I.N., aerosol and fomite exposed hamsters. Statistical significance was measured by Kruskal-Wallis test,  $n = 4$  per group.  $*P < 0.05$ ,  $**P < 0.001$ ,  $***P < 0.0001$ ,  $****P < 0.0001$ . NS, not significant. **g.** Correlation between cytokine levels, early shedding (2 DPI), peak shedding, peak weight loss, lung titers and pathology at 4 DPI. Significant correlations ( $n = 4$  per group, Pearson-Spearman analysis,  $p < 0.05$ ) are indicated with an asterisk and strength of correlation ( $R^2$ ) is depicted according to the colour bar on the right.

**Figure 5. Fomite and airborne transmission in the Syrian hamster.** **a.** Experimental layout for fomite and **b.** airborne exposure experiments in hamsters. **c.** Pictures of smoke test to demonstrate unidirectional airflow in the transmission cage. **d.** Aerodynamic particle size distribution on either side of the transmission cage. **e.** Reduction of particles by the divider. **f, g.** Relative weight loss in hamsters after SARS-CoV-2 transmission via fomite and airborne routes. Lines represent mean  $\pm$  SEM. **h.** Violin plot with individuals and median of endpoint IgG antibody titres against SARS-CoV-2 spike ectodomain by ELISA in serum of hamsters infected through airborne and fomite transmission route. ELISAs were done once. **i.** Respiratory shedding profile of hamsters exposed through fomite and airborne transmission routes, individuals, median and 95% CI are shown. **j.** cumulative (area under the curve (AUC) analysis) of respiratory shedding from animals which seroconverted after airborne and fomite transmission. Violin plots with individuals and median are depicted. Statistical significance was measured by Kruskal-Wallis test,  $n = 8$  per group.  $*P < 0.05$ ,  $**P < 0.001$ ,  $***P < 0.0001$ ,  $****P < 0.0001$ . NS, not significant.

### **Supplemental legend**

**Supplemental Figure 1: a.** Violin plot of infectious SARS-CoV-2 titer in the lungs of all animals at 14 or 21 DPI. **b.** cage and **c.** bedding contamination by infected animals till 7 DPI.

**a****b****c****d****e**



m

	Aerosol	I.N.	Fomite	Control
<b>Lung</b>				
Bronchioles	++	-	-	-
Type I	+	-	-	-
Type II	-/+	-	-	-
Mos	+	-/+	-	-
<b>Trachea</b>				
Mucosa	++	-	-	-
<b>Skull</b>				
Ciliated	++	+/++	-/+	-
Olfactory	+	-/+	-	-



